

BUBble Flow Field: a Simulation Framework for Evaluating Ultrasound Localization Microscopy Algorithms

Marcelo Lerendegui¹, Kai Riemeier¹, Bingxue Wang¹, Christopher Dunsby², and Meng-Xing Tang¹

¹Department of Bioengineering, Imperial College London, London, United Kingdom

²Department of Physics, Imperial College London, London, United Kingdom

November 2022

Abstract—Ultrasound contrast enhanced imaging has seen widespread uptake in research and clinical diagnostic imaging. This includes applications such as vector flow imaging, functional ultrasound and super-resolution Ultrasound Localization Microscopy (ULM). All of these require testing and validation during development of new algorithms with ground truth data. In this work we present a comprehensive simulation platform BUBble Flow Field (BUFF) that generates contrast enhanced ultrasound images in vascular tree geometries with realistic flow characteristics and validation algorithms for ULM. BUFF allows complex micro-vascular network generation of random and user-defined vascular networks. Blood flow is simulated with a fast Computational Fluid Dynamics (CFD) solver and allows arbitrary input and output positions and custom pressures. The acoustic field simulation is combined with non-linear Microbubble (MB) dynamics and simulates a range of point spread functions based on user-defined MB characteristics. The validation combines both binary and quantitative metrics. BUFF's capacity to generate and validate user-defined networks is demonstrated through its implementation in the Ultrasound Localisation and TRacking Algorithms for Super Resolution (ULTRASR) Challenge at the International Ultrasonics Symposium (IUS) 2022 of the Institute of Electrical and Electronics Engineers (IEEE). The ability to produce ULM images, and the availability of a ground truth in localisation and tracking enables objective and quantitative evaluation of the large number of localisation and tracking algorithms developed in the field. BUFF can also benefit deep learning based methods by automatically generating datasets for training. BUFF is a fully comprehensive simulation platform for testing and validation of novel ULM techniques and is open source.

I. INTRODUCTION

Contrast enhanced ultrasound has seen a widespread uptake in research and clinical diagnostic imaging. This includes emerging imaging modalities such as vector flow imaging, super-resolution ULM and functional ultrasound. ULM is of particular interest as it is the only imaging modality that can visualize vascular structures and flow velocity information at microscopic resolution in deep tissue *in vivo* [1]. This makes ultrasound valuable for clinical applications where tissue microvascular flow is of interest. For example, cancer research has shown that increased angiogenesis is an early event in the development of tumours [2]. In the case of atherosclerosis, which can lead to strokes and cardiac arrest, angiogenesis is the predominant form of neovascularization [3] and ULM could have the potential to be used for screening.

Most ultrasound contrast agents are highly compressible gas MBs surrounded by a lipid monolayer. MBs behave

as scatterers due to the difference in acoustic impedance between the gas and the surrounding blood. But MBs also respond non-linearly to the incident pressure wave due to their compressible gas component. Taking advantage of their non-linear response, contrast sequences such as Pulse Inversion (PI) or Amplitude Modulation (AM) allow their easy separation from regular tissue. ULM localizes isolated MBs and tracks them over many frames as they flow through the vascular network. Through the localization ULM creates sub wavelength resolution vessel representations and flow velocity maps.

The requirement for isolated bubbles poses a sparsity constraint that generates a series of limitations on the MB concentration that can be used and the total acquisition time that is needed. Improving the performance of ULM towards the goal of real-time ULM is desired. This puts the focus on providing better bubble separation and increasing the localization precision. Efforts have been made to increase the speed of ULM for example by localizing MBs at higher densities through deconvolution and multi-feature tracking [4], through sparsity-based methods [5], by splitting the bubble signal in the 3D Fourier domain [6] or through the use of phase change contrast agents [7]. However, to evaluate the large number of localisation and tracking algorithms properly, realistic datasets with ground truth are required. For ULM, such datasets should comprise realistic MB Point Spread Functions (PSFs) that coherently interact when overlapped, and the flow should reflect the structures and behavior of the clinical end-application. Datasets also need to be large and contain tens of thousands of MBs to aid in the design and network training of the increasingly popular deep learning based ULM methods [8].

There are many tools for simulating the propagation of ultrasound wave fields. Two prominent examples are Field II [9] and k-Wave [10]. There are also equations that model the behavior of MBs, and commercial tools for computing flow such as StarCCM [11]. But they are not specifically designed for ULM and they are difficult to combine. Random bivariate Gaussian curves have been used as PSFs for training Convolutional Neural Network (CNN) models [8, 12]. But these are limited due to the lack of sidelobes or bubble tails, and the interaction between overlapping PSFs is not coherent. Womersley flow has been used to perform fast simulation of flow on large vessels [13]. But this method yields results for a single

cylindrical section of a vessel, it is not a realistic model for microvasculature, and is computationally expensive to solve. There have been several attempts to model the fluctuation of a MB's radius when exposed to an incident pressure field. The most basic form is the Rayleigh-Plesset equation [14] that models a gas bubble in an infinite pool of liquid, with the limitation of its assumption that the bubble boundary moves slower than the speed of sound. Further models do consider the acoustic emission of the bubble [14], but not the behavior of the lipid monolayer. ULM normally insonifies MBs with pressure high enough to produce significant non-linear response. A more recent model added shell buckling behavior with compression and rupture on large oscillations, which considers the physical properties of the lipid monolayer and its possible buckled, elastic and broken states [15]. A more general approach was demonstrated by combining k-Wave and the Marmottant model [16]. This method included reflections and aberrations produced by the non-linear propagation on the tissue, but it is highly demanding on computing power and memory, and requires a spatial grid to be defined which affects the accuracy of the MB locations. None of the efforts so far are designed for large dataset generation, and comprise all four essential components: bubble response, acoustic fields, flow behavior and validation.

To address the shortcomings we created a fully comprehensive simulation platform for ULM, called BUFF, that incorporates arbitrary micro-vessel network generation with a quick CFD solver and linear acoustic propagation with non-linear MB dynamics and subsequent binary and quantitative evaluation for ULM algorithms. In the following we will describe how BUFF uses a custom tool to generate organic microvessel structures, how the Hagen–Poiseuille model for quick CFD simulation is calculated, how Field II as the acoustic propagation backend is combined with the Marmottant Ordinary Differential Equation (ODE) to simulate the response of the MBs and how the evaluation of ULM is achieved by means of the implementation of BUFF in the Ultrasound Localisation and TRacking Algorithms for Super Resolution (ULTRA-SR) Challenge at the IUS 2022 of the IEEE.

II. METHODS

A. Microvascular Flow

To model microvascular structures we first need to briefly define microvascular flow. The Reynolds number describes the ratio of inertial forces to viscous forces. In small vessels of the microvasculature the Reynolds number is very low and radial components of flow are zero considering that flow is laminar for $Re < 2300$

$$Re = \frac{uD}{\mu} \quad (1)$$

Where u is the flow velocity, D the vessel diameter and μ the kinematic viscosity of blood. Furthermore, such flow is quasi steady, fully developed and vessels segments are assumed to be rigid and straight. Subsequently, the axial momentum equation of the flow field derived from

the Navier Stokes equation for incompressible Newtonian fluids reduces to

$$\frac{1}{r} \frac{\delta}{\delta r} \left(r \frac{\delta u_z}{\delta r} \right) = -\frac{1}{\mu} \frac{\delta p}{\delta z} \quad (2)$$

where $\delta p / \delta z$ is the pressure as a function of the axial coordinate z and r is the radial coordinate. Imposing a no-slip condition on the wall ($u = 0$ at $r = R$) a parabolic shape of the velocity profile can be determined

$$u_z(r) = u_{z,max} \left(1 - \frac{r^2}{R^2} \right) \quad (3)$$

where $u_{z,max}$ is the maximum velocity, which is twice the mean velocity ($u_{z,mean} = 1/2 u_{z,max}$) for a parabolic (cross-sectional) flow profile

$$u_{z,max} = \frac{R^2 \Delta p}{4\mu l} \quad (4)$$

The volume flow in a vessel with finite length l can be calculated with the Hagen–Poiseuille law using the hydrodynamic resistance ξ and the pressure difference Δp .

$$Q = \frac{\pi r^4}{8\mu l} \Delta p = \frac{\Delta p}{\xi} \quad (5)$$

These basic equations of flow and pressure will be used in the network solver as a system of linear equations.

B. Network Generation

BUFF implements an organic vessel tree generation tool based broadly in a recurrent process of vasculogenesis and sprouting angiogenesis. Vessel structures are approximated as weighted directed graphs with nodes and edges. Each edge represents a cylindrical section of a vessel, with characteristics of radius, length and orientation; and each node represents the connection between two edges. The final output of this tool is a randomized binary tree structures that can be fully customized to mimic what is seen *in vivo*.

The process of network creation starts with an initial state defined by: initial position, orientation, radius, and recursion level. A vessel is created by iteratively appending new edges. Each new edge will have new randomized properties based on the current state: the rotation both in elevation and azimuth can be tuned to different vessel tortuosities, and the radius can be changed as new segments are added, creating a radius decay along the vessel. Random locations along the created vessel are chosen as 'sprouts' or locations for bifurcations, and the process is run recursively, creating new vessels at those locations. The whole process is highly customizable. This is achieved by defining parameters as functions of the current status of the generation algorithm: $param = f(n, d, e1, e2, r, lvl)$ with:

- n : the current node
- $d, e1, e2$: the current edge orientation (orthonormal reference system)
- r : the current radius
- lvl : the current recursion level

The network generation can be constraint by a global set of parameter as shown in Table I. Organs usually have

Parameter	Description
edge_step_f	step size in meters
inside_f	when to stop generating
rot_f	new orientation to use on next section of current vessel
r_decay_f	new radius to use on next section of current vessel
bif_occurs_f	whether or not a bifurcation occurs at this place
bif_r_decay_f	new radius to use on new branch vessel
bif_rot_f	new orientation to use on new branch vessel

TABLE I: The global network generation parameters can be used to constrain the network generation. For example, *edge_step_f* describes the spatial frequency of edges and *inside_f* determines the outlining 3D shape of the network.

specific shapes, and that shape limits the extent of its vessel structure. For example the *inside_f* function is used for creating specific organ shapes, by limiting the generation of vessels only to positions inside the shape.

C. Network Solver

The flow and pressure in a vessel network can be solved for every position as a system of linear equations. To construct the equations, the node-edge incidence matrix, input and output pressures, and the hydrodynamic conductance of all the edges are required. In addition, the following assumptions are made:

- fluid is incompressible
- inputs and outputs are hanging nodes
- a hanging node is connected to only one edge

Vessel networks are represented as a weighted directed graph, containing nodes and edges illustrate in Figure 1.

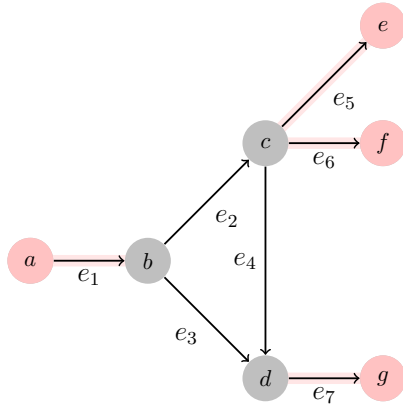


Fig. 1: Simple sample network to illustrate the relation between node (a-f) and edges (1-7). Nodes connected to only one edge are hanging nodes. Their corresponding edge is highlighted.

The incidence matrix I encodes the structure of the vessel network. The matrix I can be used to express a system of linear equations that relate the edge pressure differences and the node pressures, and another system of linear equations that relates the current at each node. The edge-node incidence matrix for the sample network is

$$\mathbf{I} = \begin{matrix} & \begin{matrix} a & b & c & d & e & f & g \end{matrix} \\ \begin{matrix} e_1 \\ e_2 \\ e_3 \\ e_4 \\ e_5 \\ e_6 \\ e_7 \end{matrix} & \begin{bmatrix} 1 & -1 & 0 & 0 & 0 & 0 & 0 \\ 0 & 1 & -1 & 0 & 0 & 0 & 0 \\ 0 & 1 & 0 & -1 & 0 & 0 & 0 \\ 0 & 0 & 1 & -1 & 0 & 0 & 0 \\ 0 & 0 & 1 & 0 & -1 & 0 & 0 \\ 0 & 0 & 1 & 0 & 0 & -1 & 0 \\ 0 & 0 & 0 & 1 & 0 & 0 & -1 \end{bmatrix} \end{matrix}$$

The pressure at the hanging nodes is known from the start, but the pressure at non-hanging nodes are unknowns that need to be solved. The incidence matrix is separated into two: I_h and I_{nh} , containing the columns of I corresponding to hanging nodes and non-hanging nodes:

$$\mathbf{I}_h = \begin{matrix} & \begin{matrix} a & e & f & g \end{matrix} \\ \begin{matrix} e_1 \\ e_2 \\ e_3 \\ e_4 \\ e_5 \\ e_6 \\ e_7 \end{matrix} & \begin{bmatrix} 1 & 0 & 0 & 0 \\ 0 & 0 & 0 & 0 \\ 0 & 0 & 0 & 0 \\ 0 & 0 & 0 & 0 \\ 0 & 1 & 0 & 0 \\ 0 & 0 & 1 & 0 \\ 0 & 0 & 0 & 1 \end{bmatrix} \end{matrix}, \mathbf{I}_{nh} = \begin{matrix} & \begin{matrix} b & c & d \end{matrix} \\ \begin{matrix} e_1 \\ e_2 \\ e_3 \\ e_4 \\ e_5 \\ e_6 \\ e_7 \end{matrix} & \begin{bmatrix} -1 & 0 & 0 \\ 1 & -1 & 0 \\ 1 & 0 & -1 \\ 0 & 1 & -1 \\ 0 & 1 & 0 \\ 0 & 1 & 0 \\ 0 & 0 & 1 \end{bmatrix} \end{matrix}$$

The pressure difference across edges can be expressed as:

$$P_e = I_h P_0 - I_{nh} P_n \quad (6)$$

with P_0 the known pressure at each hanging node, and P_n the unknown pressure at non-hanging nodes. Given the assumption that the fluid is incompressible, the sum of flows in each non-hanging node must be zero. This can be expressed as a system of linear equations:

$$I_{nh}^T Q_e = 0 \quad (7)$$

Equation 5 relates the pressure difference at the ends of an edge to the volume flow going through it. This can be expanded into a system of equations for each edge as:

$$Q_e = C P_e \quad (8)$$

with P_e , edge pressure difference vector; Q_e , Edge volumetric flow vector; and C , Edge Flow conductance Matrix

The edge conductance matrix is a diagonal matrix whose values be obtained by calculating the flow conductance at each edge, using its radius and the viscosity of the liquid on Equation 5:

$$\mathbf{C} = \begin{matrix} & \begin{matrix} e_1 & e_2 & e_3 & e_4 & e_5 & e_6 & e_7 \end{matrix} \\ \begin{matrix} e_1 \\ e_2 \\ e_3 \\ e_4 \\ e_5 \\ e_6 \\ e_7 \end{matrix} & \begin{bmatrix} \frac{1}{\xi_1} & 0 & 0 & 0 & 0 & 0 & 0 \\ 0 & \frac{1}{\xi_2} & 0 & 0 & 0 & 0 & 0 \\ 0 & 0 & \frac{1}{\xi_3} & 0 & 0 & 0 & 0 \\ 0 & 0 & 0 & \frac{1}{\xi_4} & 0 & 0 & 0 \\ 0 & 0 & 0 & 0 & \frac{1}{\xi_5} & 0 & 0 \\ 0 & 0 & 0 & 0 & 0 & \frac{1}{\xi_6} & 0 \\ 0 & 0 & 0 & 0 & 0 & 0 & \frac{1}{\xi_7} \end{bmatrix} \end{matrix}$$

Given Equation 6, Equation 7, and Equation 8 we can replace Equation 8 in Equation 7 to obtain:

$$I_{nh}^T C P_e = 0 \quad (9)$$

by replacing Equation 6 we get:

$$I_{nh}^T C (I_h P_0 - I_{nh} P_n) = 0 \quad (10)$$

$$I_{nh}^T C I_h P_0 - I_{nh}^T C I_{nh} P_n = 0 \quad (11)$$

$$I_{nh}^T C I_{nh} P_n = I_{nh}^T C I_h P_0 \quad (12)$$

which can be expressed as a linear system of equations in the form of $Mx = b$ with:

- $M = I_{nh}^T C I_{nh}$
- $x = P_n$
- $b = I_{nh}^T C I_h P_0$

This will solve for the pressure at each non-hanging node, and, using equations Equation 6, Equation 8, the volumetric flow at each edge can be derived. Note, a hanging node can be placed anywhere within the network.

D. Track generation

The bubble positions and their tracks through the network implemented through a fast track generation algorithm based three conditions:

- the probability of a bubble taking a path at a bifurcation is proportional to the flow in that path.
- bubbles move only in a streamline (they maintain their relative radial position through the whole network according to the rules of laminar flow).
- the number of bubbles is much greater than the number of all possible tracks

All possible tracks or root-to-leaf paths can be extracted from the network by computing all the combinations of paths at each vessel bifurcation. At each bifurcation, a bubble can randomly go through one of the paths. The probability of choosing one is calculated based on flow conservation and fluid incompressibility. The volume flow rate of the inlet Q_1 is the sum of its outlet Q_2 and Q_3 :

$$Q_1 = Q_2 + Q_3 \quad (13)$$

The fraction of the incoming volume that will go to branch two will then be $\frac{Q_2}{Q_1}$, so we can approximate the probability of taking that branch as:

$$p = \frac{Q_2}{Q_1} \quad (14)$$

The probability of a bubble traversing a whole track is calculated as the product of all bifurcation probabilities in a track:

$$p_{track} = \prod_{i \in T} \frac{edge_i \cdot Q}{edge_{i-1} \cdot Q} \quad (15)$$

To generate the ground truth information, any number of bubbles are moved with the network flow. For each bubble, a track is randomly chosen using the track probability calculated with Equation 15. A starting position is chosen

for the bubbles comprising both radial, angular and axial position in the starting vessel. From the starting position, a particle will move through edges at a constant speed of $edge.vel * (1 - r^2)$, with $edge.vel$ the (max) velocity at the center of the vessel, and r is the fractional radius of the streamtube the particle is traveling in. The particle position is updated using its velocity and the Δt . Once the particle reaches the end of the current edge, the overshoot is corrected and the starting position for the next edge defined:

$$pos = next_edge.start + overshoot * \frac{next_edge.vel}{cur_edge.vel} \quad (16)$$

where $next_edge.start$ is the starting location of the next edge, $next_edge.vel$ is its velocity and $cur_edge.vel$ the current edge velocity. This process is repeated until the bubble reaches the end of the track. The result of this simulation is a table of events with in the format $[frame, bubble_id, x, y, z]$. Additional parameters such as particle velocity or tube radius can be added to the table as ground truth if desired. For the final output table, all the tables from different bubbles are stacked vertically and sorted by frame number.

E. Non-linear Bubble Simulation

BUFF can solve for any ODE to obtain the response of a MB, as a default, we chose to use a modified Rayleigh–Plesset equation as follows [15]:

$$\rho_l (R\ddot{R} + \frac{3}{2}\dot{R}^2) = [P_0 + \frac{2\sigma(R_0)}{R_0}] (\frac{R}{R_0})^{-3\kappa} (1 - \frac{3\kappa}{c}\dot{R}) - P_0 - \frac{2\sigma(R)}{R} - \frac{4\mu\dot{R}}{R} - \frac{4\kappa_s\dot{R}}{R^2} - P_{ac}(t) \quad (17)$$

$$\sigma(R) = \begin{cases} 0 & \text{if } R \leq R_{buckling} \\ \chi(\frac{R^2}{R_{buckling}^2} - 1) & \text{if } R_{buckling} \leq R \leq R_{break} \\ \sigma_{water} & \text{if ruptured and } R \geq R_{ruptured} \end{cases} \quad (18)$$

This ODE is solved using Runge-Kutta methods at a higher sampling rate than the ultrasound simulation, with an user-defined oversampling factor. Solving the ODE yields the bubble radius over time and its first two derivatives: R , \dot{R} , and \ddot{R} . The scattered pressure at a distance d from the center of the bubble is defined [17]:

$$P = \frac{\rho_l}{d} (R^2 \ddot{R} + 2R\dot{R}^2) \quad (19)$$

BUFF has implementations of both a custom bubble that users can setup, and a commercial agent such as SonoVue® (sulphur hexafluoride) that is pre-configured with fitted parameters [15] as shown in Table II).

Param	Description	SonoVue
ρ_l	Density of surrounding liquid	$10^3 \frac{Kg}{m^3}$
σ_l	Surface tension of surrounding liquid	$0.073 \frac{N}{m}$
μ_l	Viscosity of surrounding liquid	$2.010^{-3} Ps$
κ	Polytropic gas exponent	1.095
κ_s	Surface dilatational viscosity from the mono-layer	$7.210^{-9} N$
χ	Elastic compression modulus of the mono-layer	$1.0 \frac{N}{m}$
R_0	Equilibrium radius of the bubble	$0.975 \mu m$
R_{buckle}	Lower radius limit of the elastic state	$0.975 \mu m$

TABLE II: Microbubble Simulation Parameters for a bubble of radius $3\mu m$

F. Integration into Linear Acoustic Simulation

Field II is a platform that simulates pressure fields from arbitrarily shaped transducers [9]. It models the ultrasound system as a Linear Time Invariant system which is characterized by its impulse response; the response to a Dirac excitation. This assumption of linearity makes Field II fast, allowing it to divide the problem into parallelizable parts, by splitting each transducer element into small mathematical sub-elements, and making every scatterer independent. Over the years, Field II's results have been shown to be accurate with ultrasound experiments [18]. The assumption of linearity is broken when incorporating the non linear dynamics of the contrast agent. To integrate bubble simulation into the FieldII's acoustic simulation, a multi step process is required. It is assumed that bubbles are independent and there is no coupling between them.

First, the transmitted pressure signal at the location of the bubble is calculated. This is done by simulating the transducer and calculating the pressure over time at the bubble location. Second, using the pressure signal calculated at step 1 as an input, we calculate the bubble response signal by using equation Equation 17 and then equation Equation 19. Finally, the bubble response signal is propagated back to the transducer. Field II does not have a direct way to calculate the signal received with the transducer when transmitting from a point source in space. This can be done by convolving the bubble response and the spatial impulse response from the bubble position to the transducer, which, because of the reversibility property of ultrasound, is equal to the impulse response from the transducer to a MB position.

$$RX(t) = \text{bub_resp}(t) * H(t, \text{bub_pos}) \quad (20)$$

G. Evaluation

The evaluation metrics of BUFF present estimations of both the fractions of correct events and the error for localization and tracking of an ULM algorithm.

a) *Localization Evaluation:* A localization is considered a True Positive (TP) if it lies close enough to a ground truth position; the localisation is inside a defined search radius centered around the ground truth location. Following this logic, a ground truth MB with no localization in its search radius is considered a False Negative (FN), and a localization that is not inside the search radius

of any ground truth False Positive (FP) location is a FP. Two metrics, *precision* and *recall* are used to indicate the fractions of the correct localisation:

$$Precision = \frac{TP}{TP + FP} \quad (21)$$

$$Recall = \frac{TP}{TP + FN} \quad (22)$$

A third metric which describes the average distance between the true position of a MB (B) and the localisation position (L) is calculated to reflect the root mean square error (RMSE) of all true positive localisation (N_{TP}):

$$RMSE = \frac{\sum_{i \in TP} \text{dist}(B_i \leftrightarrow L_i)}{N_{TP}} \quad (23)$$

b) *Tracking Evaluation:* Tracking is a process that analyzes localizations over consecutive frames and determines pairs of localizations that correspond to the same bubble. Tracking is strongly dependent on the localization performance. A bubble that was not localized will never be paired, and a FP localization should never be paired. If one were to consider all localizations for tracking, FN and FP localizations would generate a double penalty on the erroneous localizations. To separate the tracking evaluation from the localization evaluation, only true positive localizations must be considered, i.e. only pairings of correctly localized bubbles in both frames are analyzed. This diminishes the total number of pairings to work with. As the total number of localisation increases the impact of this systematic bias is reduced.

Across two consecutive frames, two paired localizations that have the same localization id are considered TP if their associated ground truth bubbles have the same bubble id. Any bubble pair that doesn't have an associated localization pair is considered a FN. Any localization pair that is not associated with a bubble pair is considered a FP. Tracking is evaluated both in fraction of correct pairs and in effective pair distance. Precision and Recall are used to indicate the fractions of correct pairings:

$$Precision = \frac{TP}{TP + FP} \quad (24)$$

$$Recall = \frac{TP}{TP + FN} \quad (25)$$

There is no direct way of measuring distance error for a pairing process. The correct pair distance can be used, i.e. the distance a bubble travels from one frame to the other. It is a fair metric, bubbles that travel further away are more difficult to track, which would yield a better result in the metric. Given that the total number of pairs is dependent on the localization process, the fraction of correct paired distance. This is equivalent to a weighted Jaccard index with the weights being the distance of each pair.

$$J = \frac{TP_d}{TP_d + FP_d + FN_d} \quad (26)$$

where:

$$TP_d = \sum_{i \in TP} \text{dist}(\text{pair}_i) \quad (27)$$

$$FP_d = \sum_{i \in FP} dist(pair_i) \quad (28)$$

$$FN_d = \sum_{i \in FN} dist(pair_i) \quad (29)$$

To provide better clarity, a remapping of this metric of the form $L = 2 * J - 1$ is used, so the range of the metric goes from $[0, 1] \rightarrow [-1, 1]$. A negative number means track is mostly wrong, and positive number is mostly right. The final metric has then the following expression:

$$J_{map} = \frac{TP_d - FP_d - FN_d}{TP_d + FP_d + FN_d} \quad (30)$$

H. BFF Validation Experiments

1) *Network Generation*: Multiple networks were generated with random parameters. In addition, a kidney and liver were mimicked to illustrate the ability of generating organic like structures with little effort. The network generator was manually constrained only by the *inside_f* to yield a similar geometric shape.

2) *Bubble Simulation*: A simulation was performed to validate BUFF's non linear simulation capabilities and replicated *in vitro*. The purpose was to test for PSFs realism and variety. The *in-vitro* experiment was done with an L11-5v 128-element linear array transducer with a transmitted frequency of 7 MHz. Perfluorobutane MBs were created following the process described in [19], and placed in a beaker with de-gassed, filtered water at room temperature. Images were acquired with a Verasonics Vantage 256 platform (Verasonics Inc., Redmond, WA). Plane wave imaging compounding using three angles and a transmission amplitude corresponding to a Mechanical Index (MI) of 0.05 was used. The simulation replicated the transducer, and MBs with random parameters and locations. The resulting images were visually assessed and PSFs of similar morphology were identified and extracted.

3) *ULTRA-SR Challenge*: BUFF's qualities were demonstrated at the ULTRA-SR challenge at the IUS 2022 of the IEEE. Contrast enhanced ultrasound videos from four randomly generated networks with ground truth were produced for this competition. The proposed evaluation criteria were used for objective and quantitative evaluation of the participants localisation and tracking algorithms. The synthetic data was created using networks with varying density on different spatial sections. To minimize the predictability of the path of a MB the vessel tree generation parameters e.g., bifurcation probability, angle between consecutive segments or MB seeding probability were randomized. A training dataset was also provided with a single branch with a low MB concentration. The competition data combined multiple branching vessel trees into a single network with high MB concentration.

III. RESULTS

A. Network Generation

Figure 2 (A) shows randomly generated networks with a different number of maximum allowed recursion levels.

The vessels are color coded according to their size. Different amount of tortuosity and three-dimensionality are demonstrated with complexity of the network increasing from left to right. Networks are constrained e.g. by the *inside_f* function to a rectangular shape. Figure 2 (B, C) shows the ability of BUFF to generate physiological shapes based on such simple constraints. BUFF is used to generate a network closely resembling the coronary microvasculature (B) and the shape of a kidney (C). The parameterised generation of networks can generate any arbitrary shape.

B. Network Seeding

Figure 3 shows the seeding of a randomly generated network along the tracks with a bubble radial position $r=0$.

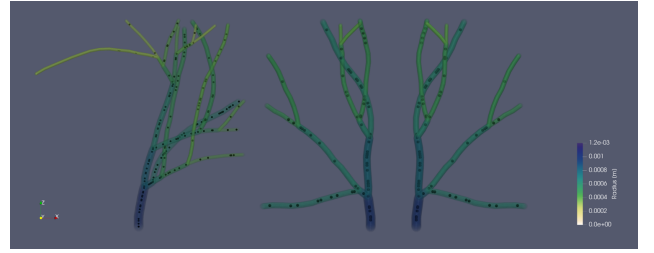


Fig. 3: Particles seeded on the network

C. Bubble Simulation

BUFF's parameterised bubble generation results in a variety of shapes of the point spread function associated with a MB. Figure 4 qualitatively shows the difference in the B-Mode image between simulated MBs (B, D) and MBs from an *in vitro* beaker acquisition (A, C). The mono-lobe (A, B) and multi-lobe (C, D) morphological shapes are distinct from each other. The side lobe signal is stronger in the simulation compared to the *in vitro* experiment.

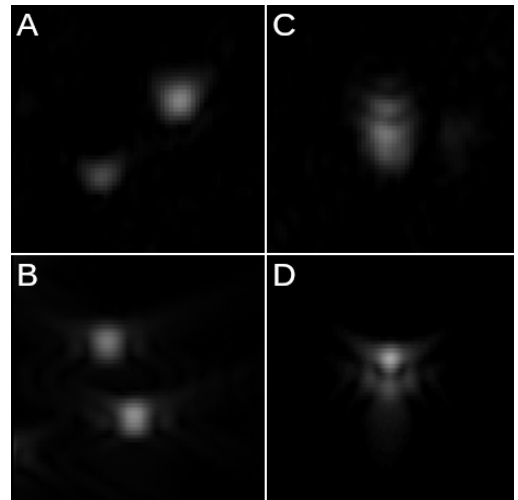


Fig. 4: Comparison between PSF morphology seen in simulation and *in vitro*. **A & C**: Mono-lobe and multi-lobe morphologies observed at *in vitro* beaker experiments. **B & D**: Mono-lobe and multi-lobe morphologies can also be observed when recreating the experiment using BUFF.

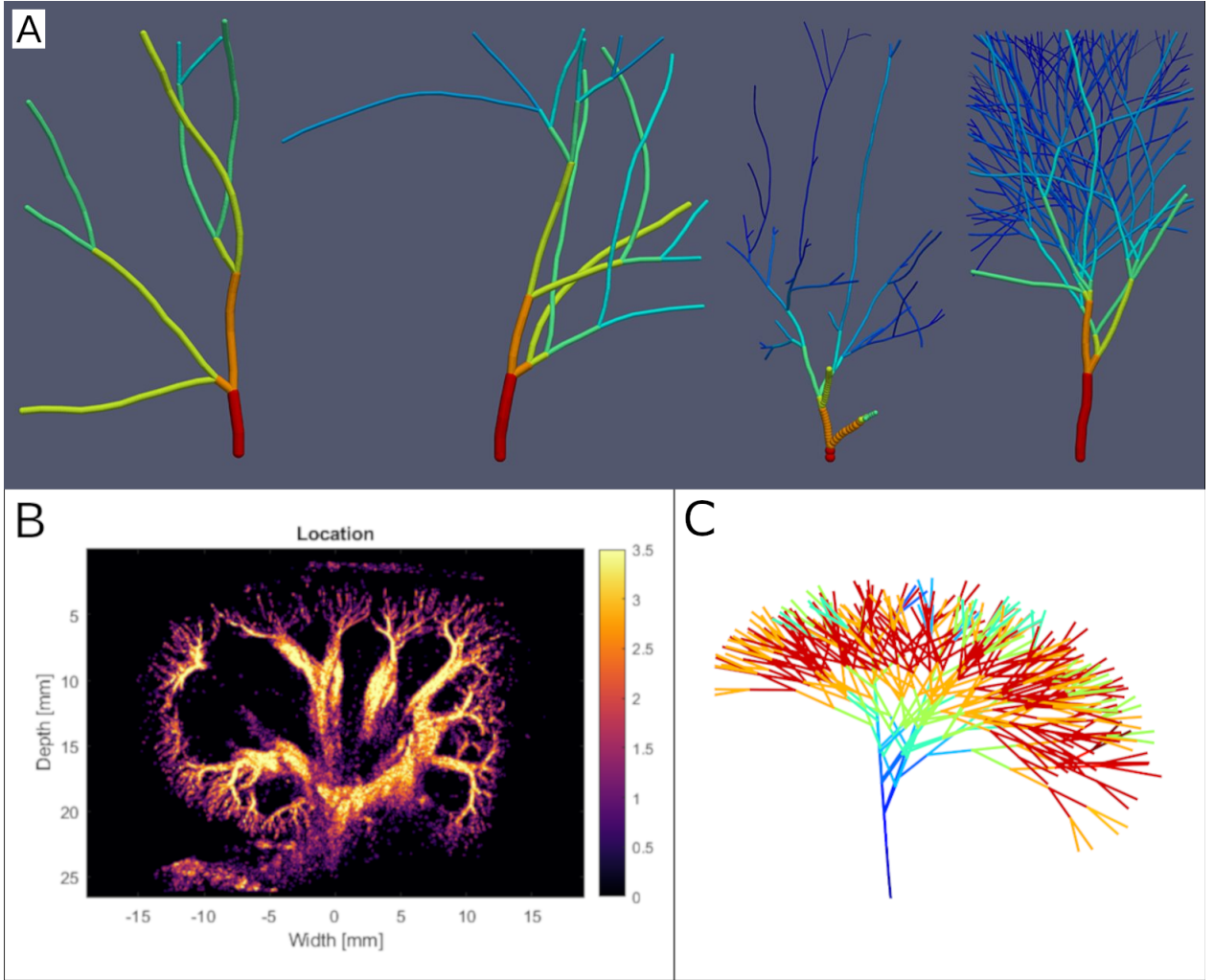


Fig. 2: **A:** Randomly generated networks obtained using different maximum allowed recursion levels. Recursion level from left to right: lvl=2, lvl=3, lvl=4, lvl=5. Rectangular constraint on network shape. **B:** Superresolution Ultrasound Image of a Rabbit Kidney[7]. **C:** Generated Network mimicking the ramifications of one of the interlobar arteries of the rabbit's kidney.

D. ULTRA-SR Challenge

Two randomly generated networks of MB seeded vessel trees (Figure 5) were simulated using BUFF as shown in Figure 5. The final networks were generated from multiple smaller networks to make localization and tracking difficult. No apparent structure within the networks is recognisable. Figure 6 shows the B-Mode images of both networks. It demonstrates the effect of adding *Additive Colored Noise* and *Gaussian White Noise* to the beamformed radio frequency signals. Through a *Time Gain Compensation* the signal to noise ratio decreases with depth. The signal to noise ratio is higher in the low frequency dataset (Figure 6, B) compared to the higher frequency dataset (Figure 6, A).

Figure 7 shows the B-Mode frames, superimposed with both the ground truth locations and the predicted locations. The two expanded regions show in detail how accurate the predictions are. The presence of FN (isolated green cross) locations can be appreciated in both the High Frequency (HF) and Low Frequency (LF) images. Additionally, both images (C & D) show two neighbouring bubbles being identified as one.

The final superresolution image and its velocity map

are shown in Figure 8 and Figure 9. While the observed network resembles the one presented in Figure 5, the density of tracks is not the same, and large black gaps can be seen. This result is expected when the localization and tracking results (Table III) are taken into consideration. For the HF dataset, a precision= 0.51 indicates that around 50% of the true localizations was not captured, and of the possible pairings to be made with the correctly localized positions, only 43% were actually paired. On the other hand, the results also show a high tracking precision of 0.99 for the HF dataset, which means that only 1% of the tracks present in the final image will be inexistent lines created by the algorithm. The performance of the algorithm is worse for the LF dataset despite the higher signal to noise ratio. This was expected because of its much larger psf.

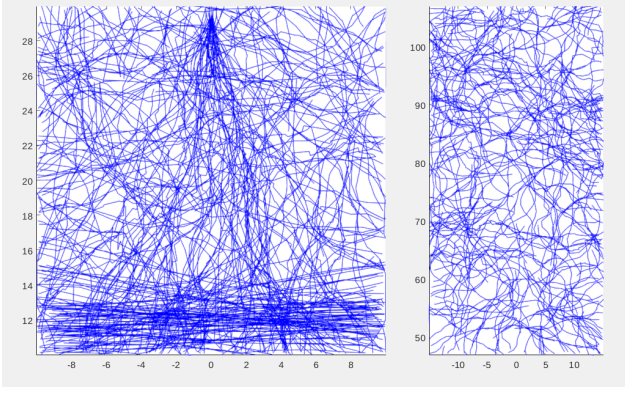


Fig. 5: Structures generated with BUFF for the ULTRA-SR. **A:** The vessel network for the HF simulation. **B:** The vessel network for the LF simulation

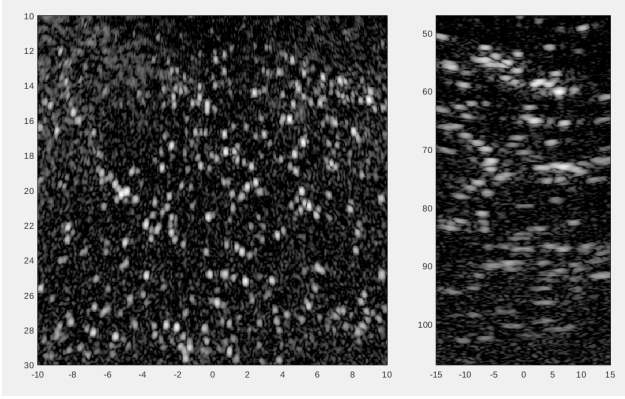


Fig. 6: Generated B-Mode frames. **A:** Frame N149 of the HF video simulation. **B:** Frame N4 of the LF video simulation

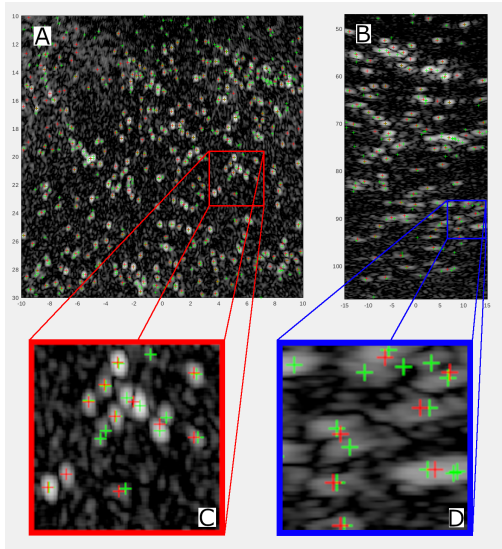


Fig. 7: Superposition of a B-Mode frame and the bubble localizations. The ground truth is shown as a green cross, and the algorithm output is shown as a red cross. **A & C:** HF video frame N149 and detail of a region. **B & D:** LF video frame N4 and detail of a region.

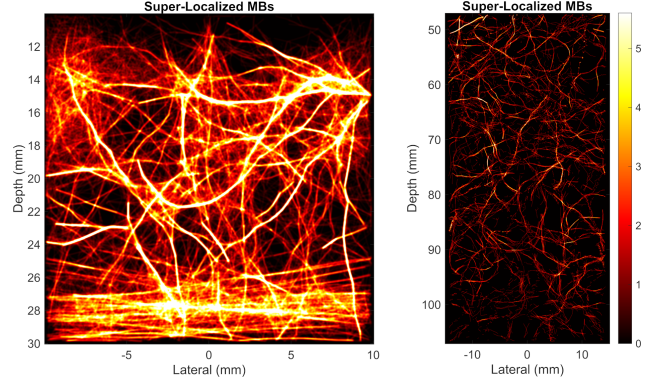


Fig. 8: Resulting SR Images obtained from localization and tracking. **A:** HF network. **B:** LF network

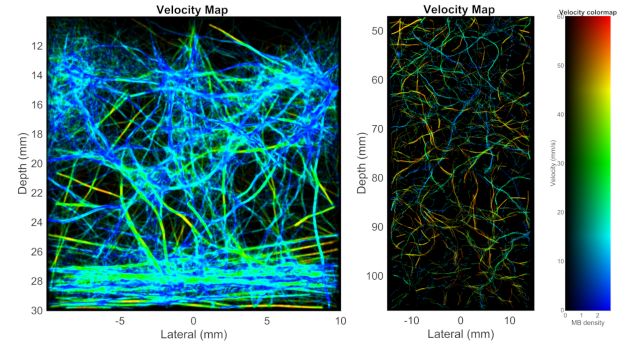


Fig. 9: Resulting Velocity Map Image obtained from tracking. **A:** HF network. **B:** LF network

Localization		Localization	
Precision	0.48	Precision	0.74
Recall	0.51	Recall	0.66
RMSE	135.79 μm	RMSE	47.34 μm
Tracking		Tracking	
Precision	0.99	Precision	0.56
Recall	0.43	Recall	0.44
J_{map}	-0.71	J_{map}	-0.57

(a) Low Frequency

(b) High Frequency

TABLE III: Evaluation results

IV. DISCUSSION

We developed BUFF, a fully comprehensive simulation platform for ULM algorithm development and evaluation. The framework consists of four key components: a microvascular structure generator, a flow simulator, an acoustic field simulator coupled with nonlinear microbubble dynamics and an evaluation pipeline for binary and quantitative assessment. The framework code is object oriented which makes it modular and easy to extend. BUFF allows the user to create short, concise and powerful scripts that simulate dynamic MBs excited by common ultrasound transducers and is open source.

The microvessel structure generator can be customized to yield networks that resemble realistic vascular structures, Figure 2.A shows how parameters like the recursion

level, can generate models with increasing vessel densities. Organic structures like the vessels structures seen on kidneys, can be replicated. Figure 2.B shows how the ramifications of interlobar arteries of the rabbit's kidney can mimicked. To this point, only binary trees Figure 2 are capable of being generated, but the implementation can be extended to generate other networks. The addition of loop connections could help mimic intussusceptive angiogenesis for even more realistic structures.

The incorporation of non-linear simulation of MBs via Modified Rayleigh–Plesset ODEs has proven to generate realistic PSFs (Figure 4) and enable simulation of coded transmission techniques such as AM. The simulation not only is realistic in terms of the shapes and sizes of the resulting PSFs, but also realistic RadioFrequency (RF) data is generated. This means that the datasets generated using BUFF can be used to assess algorithms and techniques that require that type of input, for example beamforming.

BUFF helps address one important problem present in ULM algorithm creation, evaluation and validation: the creation of realistic microvascular phantoms and data with ground truth. The realism of BUFF's simulations greatly facilitate the evaluation of ULM algorithms, and the datasets generated by BUFF framework has been used by the ULTRA-SR challenge (<https://ultra-sr.com>) at the IEEE IUS 2022 to evaluate a number of localisation and tracking algorithms.

Even though this work focuses on ULM as a proof of concept, BUFF is not limited to this application only. Any contrast imaging related application can greatly benefit from datasets with ground truth for evaluation. Additionally, the accurate flow simulation is of special interest for applications like Ultrasound Vector Flow Imaging or Perfusion Imaging.

Data driven algorithms such as deep learning methods will benefit from this framework thanks to its compute time which is adequate for large dataset generation. The most time consuming step in the simulation framework is the acoustic field simulation. For the purpose of keeping it as open-source BUFF uses the free version of FieldII[9], further speed up can be achieved by using the commercial version. It should be noted that Field II does not simulate non-linear propagation of ultrasound. However, given the low mechanical index used for MB imaging, the effect of nonlinear propagation, particularly when bubbles are excited at resonance frequency, is low [20].

V. CONCLUSION

This work introduces BUFF, a simulation framework for algorithm development and evaluation, with a focus on fast and large dataset creation, which will simplify the development and assesment of deep learning models and traditional algorithms for all the stages in the ULM pipeline. As a proof of concept, BUFF was used for the ULTRA-SR competition at IEEE IUS 2022, proving that it can create random organic networks that resemble physiological structures seen in-vivo, it can yield flow simulations that are accurate representation so of actual microvascular flow, it uses simulation of MB dynamics to generate realistic PSFs that resemble the ones seen on

experiments, and it is suitable for large dataset generation thanks to its speed.

VI. ACKNOWLEDGEMENTS

This work was supported by UK Engineering and Physical Sciences Research Council (EPSRC).

The complete simulated dataset for ULTRA-SR can be found on <https://doi.org/10.5281/zenodo.7271766>

REFERENCES

- [1] M. Dewey, M. Siebes, M. Kachelrieß, *et al.*, “Clinical quantitative cardiac imaging for the assessment of myocardial ischaemia,” en, *Nature Reviews Cardiology*, vol. 17, no. 7, pp. 427–450, Jul. 2020.
- [2] J. Laitakari, V. Näyhä, and F. Stenbäck, “Size, shape, structure, and direction of angiogenesis in laryngeal tumour development,” *Journal of Clinical Pathology*, vol. 57, no. 4, pp. 394–401, Apr. 2004.
- [3] *Neovascularization in Human Atherosclerosis*, en.
- [4] J. Yan, T. Zhang, J. Broughton-Venner, *et al.*, “Super-Resolution Ultrasound Through Sparsity-Based Deconvolution and Multi-Feature Tracking,” eng, *IEEE transactions on medical imaging*, vol. 41, no. 8, pp. 1938–1947, Aug. 2022.
- [5] A. Bar-Zion, O. Solomon, C. Tremblay-Darveau, *et al.*, “SUSHI: Sparsity-Based Ultrasound Super-Resolution Hemodynamic Imaging,” *IEEE Transactions on Ultrasonics, Ferroelectrics, and Frequency Control*, vol. 65, no. 12, pp. 2365–2380, Dec. 2018, Conference Name: IEEE Transactions on Ultrasonics, Ferroelectrics, and Frequency Control.
- [6] C. Huang, M. R. Lowerison, J. D. Trzasko, *et al.*, “Short Acquisition Time Super-Resolution Ultrasound Microvessel Imaging via Microbubble Separation,” en, *Scientific Reports*, vol. 10, no. 1, p. 6007, Apr. 2020.
- [7] K. Riemer, M. Toulemonde, J. Yan, *et al.*, *Fast and selective super-resolution ultrasound in vivo with sono-switchable nanodroplets*, arXiv:2203.04263 [eess], Mar. 2022.
- [8] R. J. G. van Sloun, O. Solomon, M. Bruce, *et al.*, “Super-Resolution Ultrasound Localization Microscopy Through Deep Learning,” eng, *IEEE transactions on medical imaging*, vol. 40, no. 3, pp. 829–839, Mar. 2021.
- [9] J. Jensen, “FIELD: A program for simulating ultrasound systems,” *Medical and Biological Engineering and Computing*, vol. 34, pp. 351–352, Jan. 1996.
- [10] B. E. Treeby and B. T. Cox, “K-Wave: MATLAB toolbox for the simulation and reconstruction of photoacoustic wave fields,” eng, *Journal of Biomedical Optics*, vol. 15, no. 2, p. 021314, Apr. 2010.
- [11] S. D. I. Software, *Simcenter STAR-CCM+*, 2021.
- [12] X. Liu, T. Zhou, M. Lu, *et al.*, “Deep Learning for Ultrasound Localization Microscopy,” *IEEE Transactions on Medical Imaging*, vol. 39, no. 10, pp. 3064–3078, Oct. 2020, Conference Name: IEEE Transactions on Medical Imaging.

- [13] K. Riemer, E. M. Rowland, J. Broughton-Venner, *et al.*, “Contrast Agent-Free Assessment of Blood Flow and Wall Shear Stress in the Rabbit Aorta using Ultrasound Image Velocimetry,” en, *Ultrasound in Medicine & Biology*, vol. 48, no. 3, pp. 437–449, Mar. 2022.
- [14] M. Versluis, E. Stride, G. Lajoinie, *et al.*, “Ultrasound Contrast Agent Modeling: A Review,” en, *Ultrasound in Medicine & Biology*, vol. 46, no. 9, pp. 2117–2144, Sep. 2020.
- [15] P. Marmottant, S. Meer, M. Emmer, *et al.*, “A model for large amplitude oscillations of coated bubbles accounting for buckling and rupture,” *Journal of The Acoustical Society of America - J ACOUST SOC AMER*, vol. 118, pp. 3499–3505, Dec. 2005.
- [16] J. Brown, K. Christensen-Jeffries, S. Harput, *et al.*, “Investigation of Microbubble Detection Methods for Super-Resolution Imaging of Microvasculature,” eng, *IEEE transactions on ultrasonics, ferroelectrics, and frequency control*, vol. 66, no. 4, pp. 676–691, Apr. 2019.
- [17] K. Vokurka, “On Rayleigh’s model of a freely oscillating bubble. I. Basic relations,” en, *Czechoslovak Journal of Physics B*, vol. 35, no. 1, pp. 28–40, Jan. 1985.
- [18] J. Jensen and N. Svendsen, “Calculation of pressure fields from arbitrarily shaped, apodized, and excited ultrasound transducers,” *IEEE Transactions on Ultrasonics, Ferroelectrics, and Frequency Control*, vol. 39, no. 2, pp. 262–267, Mar. 1992, Conference Name: IEEE Transactions on Ultrasonics, Ferroelectrics, and Frequency Control.
- [19] J. Hansen-Shearer, M. Lerendegui, M. Toulemonde, *et al.*, “Ultrafast 3-D Ultrasound Imaging Using Row-Column Array-Specific Frame-Multiply-and-Sum Beamforming,” *IEEE Transactions on Ultrasonics, Ferroelectrics, and Frequency Control*, vol. 69, no. 2, pp. 480–488, Feb. 2022, Conference Name: IEEE Transactions on Ultrasonics, Ferroelectrics, and Frequency Control.
- [20] M.-X. Tang, N. Kamiyama, and R. J. Eckersley, “Effects of Nonlinear Propagation in Ultrasound Contrast Agent Imaging,” en, *Ultrasound in Medicine & Biology*, vol. 36, no. 3, pp. 459–466, Mar. 2010.